ChemComm

COMMUNICATION

Check for updates

MOF-on-MOF heterojunction-derived Co$_3$O$_4$–CuCo$_2$O$_4$ microflowers for low-temperature catalytic oxidation†

Jingwen Mao,[a] Qin Meng, [ID] [b] Zehai Xu,[a] Lusheng Xu,[a] Zheng Fan[a] and Guoliang Zhang [ID] *[a]

Through the exchange-extended growth method (EEGM), MOF-on-MOF heteroarchitectures with distinct crystallography were produced and pyrolyzed into hybrid metal oxides. The strong exchange ability of organometallic compounds realized the component reconstruction of the MOF matrix and enhanced the interfacial forces between MOFs, showing an excellent performance in low-temperature catalytic oxidation.

Metal–organic frameworks (MOFs), as a class of organic–inorganic hybrid materials with a high specific surface area, tailorable porosity and designable molecular structures, have been widely used in gas adsorption and separation, gas sensing and heterogeneous catalysis.[1] In recent years, conventionally prepared MOFs with single structures have been unable to effectively meet some practical needs. To make up for this deficiency, the combination of MOFs with other functional materials, such as inorganic nanoparticles, carbon nanotubes, polymers and other MOFs, to construct hybrid MOF materials can extend the functionality of MOF materials.[2] In particular, blending a MOF with another MOF to form a hierarchical "MOF-on-MOF" structure utilize the advantages of MOFs with diverse structures, which can improve their performance and extend their application prospects.

So far, various synthetic approaches have been developed to construct hierarchical MOFs with different structures, such as the template and etching method, the post-synthesis method, epitaxial growth, the internal extended growth method, *etc.*[3] Most hybrid MOF-on-MOF structures have been established

[a] Institute of Oceanic and Environmental Chemical Engineering, Center for Membrane and Water Science &Technology, Zhejiang University of Technology, Hangzhou, 310014, China. E-mail: guoliangz@zjut.edu.cn; Fax: +86 571 88320863; Tel: +86 571 88320863

[b] College of Chemical and Biological Engineering, State Key Laboratory of Chemical Engineering, Zhejiang University, Hangzhou, 310027, China

† Electronic supplementary information (ESI) available: Experimental details, SEM, TEM, XRD, XPS characterization, and catalytic performance of CO oxidation. See DOI: https://doi.org/10.1039/d2cc04954f

between MOF materials with similar crystal topologies or similar linking ligands. For example, core–shell of MIL-88B@MIL-88A, with similar three-dimensional hexagonal structures, was synthesized using the template method.[4] Hierarchical FeNiZn-MIL-88B-on-MOF-5 octapods with the same linking ligand were produced using the phase-competition-driven growth method, and displayed high selectivity for the RWGS reaction.[5] Moreover, Co$_3$O$_4$/CNTs derived from core–shell Zn/Co MOFs, and Co–C@Cu–C derived from Co-MOF-74@Cu-MOF-74 with well-matched crystal lattices, have both shown good catalytic activity.[6] Many studies have shown that the construction of a hybrid MOF-on-MOF effectively improved the reactivity of the materials. However, owing to the fact that most MOFs have different components and crystal topologies, high interfacial energies may hinder the construction of MOF-on-MOF structures. The generation of well-defined hybrid MOFs from two MOFs with different components and crystal topologies *via* anisotropic MOF-on-MOF growth is quite challenging but significant.

Herein, we have developed a novel and facile exchange-extended growth method (EEGM) to construct a series of MOF-on-MOF materials, overcoming the limitation of lattice matching rule (Fig. 1). In implementing the EEGM, two MOFs
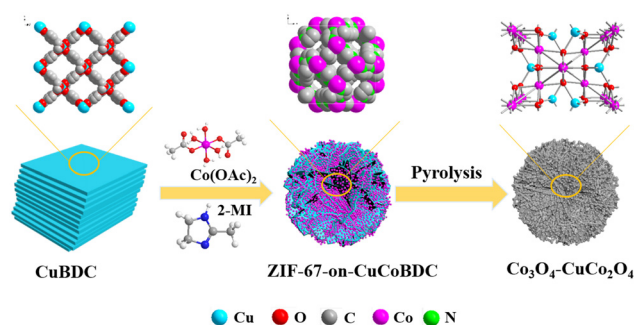

Fig. 1 Schematic representation of the preparation of hybrid Co$_3$O$_4$–CuCo$_2$O$_4$ derived from ZIF-67-on-CuCoBDC.

with completely different compositions and topologies, namely CuBDC and ZIF-67 (Fig. S1, ESI†), can be well hybridized into MOF-on-MOF heterostructures through a hydrothermal process where CuBDC is exposed to the ZIF-67 precursor with an organometallic compound as the metal source. The cobalt acetate molecules partially replaced Cu^{2+} at the CuBDC node, resulting in the transformation of CuBDC to CuCoBDC. After a simple solvothermal reaction, many dodecahedral ZIF-67 particles were uniformly dispersed on the CuCoBDC nanosheets. The specific synthesis process can be described via chemical equations (Fig. S2, ESI†). Serving as the sacrificial template, hybrid spinel oxides were synthesized by annealing this hetero MOF-on-MOF through simultaneous MOF decomposition and metal oxidation in air for crystallization. Benefitting from the hierarchically structured MOF composites, the hybrid spinel oxides with a higher BET specific area and abundant composition exhibited an excellent catalytic performance in low-temperature catalytic oxidation. Compared with other reported methods, the strategy of in situ coordination following organometallic compound exchange can fundamentally overcome the difficulty of insufficient interaction between the MOFs due to their interface mismatch, and produce more stable MOF-on-MOF heterojunctions, which can be extended to the fabrication of more advanced spinel oxides for versatile applications.

Through a solvothermal reaction with the precursor solution of ZIF-67, layer-stacked CuBDC was transformed into hybrid ZIF-67-on-CuCoBDC microflowers, which displayed a three-dimensional hierarchical microstructure with an average size of 20.0 μm (Fig. 2a–c). The structure of the hybrid microflower was further verified by TEM images and SEM mapping (Fig. S3a and S4a, ESI†). The obtained ZIF-67-on-CuCoBDC was calcined to generate crystalline hybrid Co_3O_4–$CuCo_2O_4$. During this thermal crystallization process, simultaneous decomposition

and oxidation processes promoted the formation of different crystalline oxides, in which ZIF-67 was pyrolyzed to Co_3O_4 and CuCoBDC was pyrolyzed to spinel $CuCo_2O_4$. The microflower morphologies of Co_3O_4–$CuCo_2O_4$ were well preserved even after pyrolysis (Fig. 2d and e), which indicated that the MOF-on-MOF hybrid materials synthesized via the EEGM strategy had good structural stability and can successfully prevent the possible collapse or aggregation of the hybrid structure during the pyrolysis process. HRTEM images indicate the high crystallinity of the Co_3O_4–$CuCo_2O_4$ microflowers (Fig. 2f–h). The lattice spacings of 0.244, 0.286, 0.469 nm can be attributed to the (311), (220), (111) planes, respectively, of Co_3O_4 or $CuCo_2O_4$.[7] STEM elemental mapping further displays the uniform distribution of the characteristic elements (Fig. S4b, ESI†).

The formation mechanism of ZIF-67-on-CuCoBDC was investigated by comparing the morphologies and structures of the solvothermal products of cobalt acetate and CuBDC (i.e., CuCoBDC), and 2-methylimidazole and CuBDC (i.e., CuBDC-MI). The formation process of the hybrid MOF-on-MOF structures can be grouped into two steps: exchange of cobalt acetate molecules, and in situ extended growth of ZIF-67 (Fig. 3a). The sheet-like morphology of CuBDC was transformed after the solvothermal reaction with $Co(OAc)_2$. The original two-dimensional nanosheets self-assembled to form a three-dimensional flower-like structure, and the square nanosheets gradually tended to be fusiform (Fig. S5a and b, ESI†). However, the morphology of the solvothermal product of CuBDC and 2-MI did not change significantly and it was still a stacked sheet, but due to the basicity of imidazole, the sheets were stacked more tightly (Fig. S5c and d, ESI†). The strong exchange action between the organometallic compound and the MOF host leads to faster exchange of Co^{2+} with Cu^{2+} at framework nodes.[8] The structural state of CuCoBDC was further analyzed via TEM (Fig. S6a, ESI†). Interestingly, it can be observed from the HRTEM images that some lattice fringes appeared on the CuCoBDC surface that are absent from the CuBDC surface
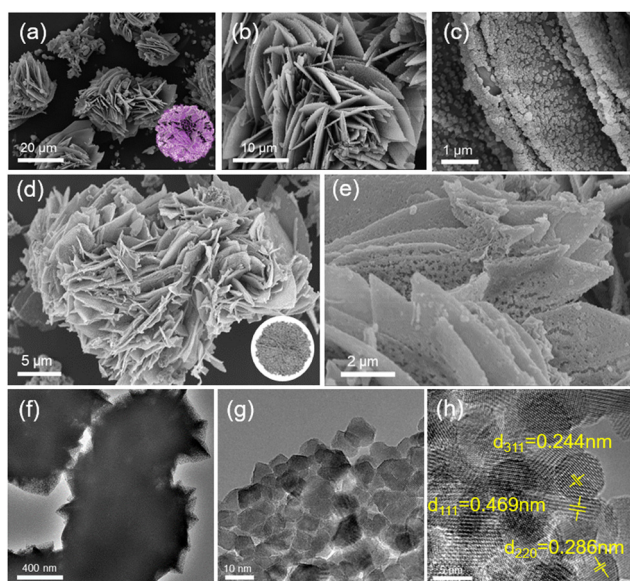

Fig. 2 SEM images of ZIF-67-on-CuCoBDC (a–c). SEM images of Co_3O_4–$CuCo_2O_4$ (d and e). TEM and HRTEM images of Co_3O_4–$CuCo_2O_4$ (f–h).
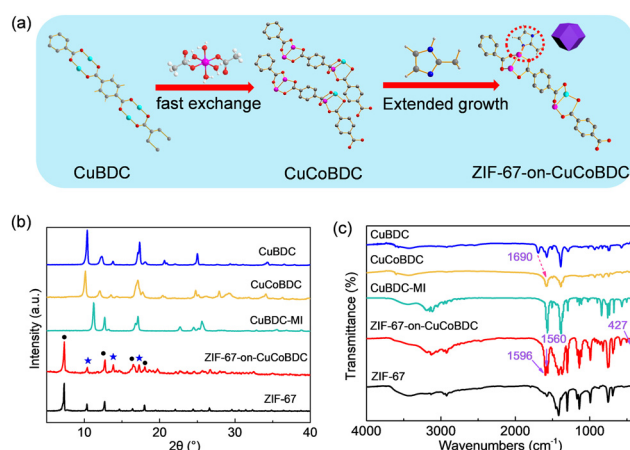

Fig. 3 Structural representation of the exchange-extended growth associated with the systematic growth of the MOF-on-MOF hybrid structure (a). XRD patterns (b) and FTIR spectra (c) of CuBDC, CuCoBDC, CuBDC-MI, ZIF-67-on-CuCoBDC and ZIF-67.

(Fig. S6b, ESI†). This is due to the low ionization properties of cobalt acetate, which can coordinate with the solvent to form a complex and adsorb on the surface of CuCoBDC. Moreover, spot scan analysis of the sheet and dodecahedral particle structure of ZIF-67-on-CuCoBDC was conducted (Fig. S7, ESI†). As expected, the spot scan on the sheet showed the presence of Co and Cu elements, indicating the successful exchange of cobalt acetate, while the spot scan on the dodecahedral particle showed N and Co elements, indicating the *in situ* growth of ZIF-67.

XRD analysis was carried out to confirm the crystal structure of the prepared ZIF-67-on-CuCoBDC (Fig. 3b). The main characteristic peaks of the produced samples matched well with the XRD patterns of CuCoBDC and ZIF-67 (Fig. 3b), which confirmed the well-defined MOF-on-MOF structure. For the obtained MOF-on-MOF composites, the (011), (112), (013), and (222) crystal faces in ZIF-67 and the characteristic lattice planes with 2θ of $10.24°$, $13.7°$ and $17.26°$ in CuCoBDC co-exist in the associated XRD patterns. This revealed the integrity of the crystal composition of ZIF-67 and CuCoBDC after combination. Moreover, the peak intensity of CuCoBDC upon hybridization was relatively weak. These results convincingly revealed the epitaxial growth of ZIF-67 on CuCoBDC. When the obtained ZIF-67-on-CuCoBDC was calcined at 300 °C for 2 h in an air atmosphere, the XRD pattern of the obtained black powder shows peaks assigned to Co_3O_4 with a hexagonal structure (JCPDS: 42-1467) as well as distinct peaks related to the cubic spinel structure of $CuCo_2O_4$ (JCPDS: 36-1189) without any other impure phases (Fig. S8, ESI†).

The FTIR spectra of ZIF-67-on-CuCoBDC is shown in Fig. 3c. It was observed that only the CuBDC spectrum had a characteristic peak at 1690 cm^{-1}, which is attributed to the –COOH vibration peak of H_2BDC, while it disappeared in CuCoBDC and ZIF-67-on-CuCoBDC, confirming that molecular $Co(OAc)_2$ was further coordinated with H_2BDC. As for ZIF-67-on-CuCoBDC, two peaks appear at 1596 and 1560 cm^{-1}, which may be due to the partial substitution of Cu^{2+} by Co^{2+}, causing the O atoms of the carboxylate groups to connect with two different metal atoms.[9] Moreover, the stretching vibrational peaks located at 427 cm^{-1} correspond to Co–N bonds, and other bands in the range of 600–1500 cm^{-1} are related to the stretching and bending modes of the imidazole ring.[10] All of these characteristic peaks can be found in the ZIF-67-on-CuCoBDC material, which offers powerful evidence for the presence of ZIF-67 and CuCoBDC in ZIF-67-on-CuCoBDC. The presence of C, N, O, Cu and Co can be ascertained in the XPS spectra of ZIF-67-on-CuCoBDC (Fig. S9, ESI†). In addition, it can be found that the binding energy of Cu 2p in this product is slightly decreased, while that of Co 2p is slightly increased relative to the single component, which is also consistent with the process result of Co^{2+} partially replacing Cu^{2+} (Fig. S10, ESI†).[11]

Moreover, not only was ZIF-67 synthesized on the CuCoBDC material *via* EEGM, but also the production of MOF-on-MOF materials was successfully achieved on other carboxylic acid-type MOF substrates using this method to optimize the design of a novel multicomponent MOF system, including bivalent/trivalent MOF heteroarchitectures (ZIF-67-on-MIL-53 (AlCo), ZIF-67-on-MIL-53 (FeCo)) and bivalent/tetravalent MOF heteroarchitectures (ZIF-67-on-UiO-66 (ZrCo)) (Fig. S11 and S12, ESI†). The relevant XRD patterns confirmed the formation of heterogeneous structures (Fig. S13, ESI†).

Since the calcination temperature has a significant effect on the performance of the MOF derivatives, TGA was performed on ZIF-67-on-CuCoBDC (Fig. S14, ESI†). In a nitrogen atmosphere, ZIF-67-on-CuCoBDC was relatively stable at 300 °C with a weight loss of about 10.03%, which was related to the removal of surface adsorbed water. The weight loss increased and eventually stabilized to 26.43% at about 700 °C. By contrast, under an air atmosphere, ZIF-67-on-CuCoBDC started to decompose around 200 °C, the weight loss was 40.58 wt% at 300 °C, and it had decomposed completely at 337 °C. Combined with the performance comparison of catalysts prepared at different calcination temperatures (Fig. S15, ESI†), 300 °C was chosen as the thermal decomposition temperature. XPS for Co_3O_4–$CuCo_2O_4$ was further performed (Fig. S16, ESI†). The C 1s spectrum was dominated with binding energy peaks at 284.6, 288.3, 289.2 and 290.3 eV, which were assigned to C=C, N=C–N, C=O and O–C=O groups, respectively. N 1s binding energies at 398, 399.1 and 400.1 eV showed that pyrrolic-N, pyridinic-N and graphitic-N were the dominant N species.[12] In particular, graphite carbon and graphite nitrogen were the key factors to effectively improve the molecular adsorption and accelerate the catalytic process.

In this work, taking CO oxidation as an example, the catalytic properties of hybrid Co_3O_4–$CuCo_2O_4$ were studied. As depicted in Fig. 4a, CuO and Co_3O_4 derived from CuBDC and ZIF-67 completely converted CO into CO_2 at 240 and 130 °C, respectively, showing that Co sites offered a greater contribution to the catalytic oxidation. As expected, the derived Co_3O_4–$CuCo_2O_4$ completely oxidized CO at 100 °C. Mechanically mixed derivatives of ZIF-67/CuCoBDC and ZIF-67/CuBDC were also tested (Fig. S17, ESI†). Co_3O_4/$CuCo_2O_4$ and Co_3O_4/CuO completely converted CO at 115 and 135 °C, respectively, showing that the hybridization of Co_3O_4 and $CuCo_2O_4$ improved the catalytic activity. In addition, Co_3O_4–$CuCo_2O_4$ still had a higher catalytic effect than the derived catalyst of CuCoBDC (100% CO conversion at 115 °C). This is because the hybrid material has a higher specific surface area than other
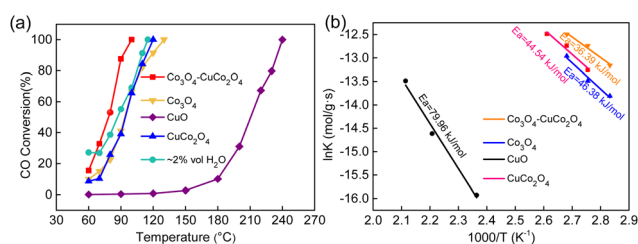

Fig. 4 CO conversion of CuO derived from CuBDC, Co_3O_4 derived from ZIF-67, $CuCo_2O_4$ derived from CuCoBDC, Co_3O_4–$CuCo_2O_4$ derived from ZIF-67-on-CuCoBDC, and the catalytic activities of Co_3O_4–$CuCo_2O_4$ for CO oxidation under moisture-rich conditions ($\sim$2% H_2O) (a). Corresponding Arrhenius plots for the reaction kinetics (b).

catalysts, which is more conducive to the adsorption and catalysis of molecules on the surface (Fig. S18, ESI†).

In the experiment, 2.0 vol% water vapor was introduced to verify its water resistance. Compared with the dry environment, the complete conversion temperature was only reduced by 15 °C, and after a continuous flow of water for 12 h, the CO conversion rate was not lowered (Fig. S19a, ESI†). The effect of H_2O on the reversibility of the catalyst was also tested (Fig. S19b, ESI†),[12,13] and it was shown that the conversion rate of CO increased rapidly to nearly 100% after introducing water vapor, but with the continuous input, the CO conversion decreased and finally remained at about 55%. After the withdrawal of water vapor, the conversion efficiency of CO gradually increased to 80% and remained stable. The interesting phenomenon is consistent with results reported previously, because at moderate temperatures the adsorption of water vapor on the catalyst surface causes a negative apparent activation energy.[14,15]

The lowest apparent activation energy (36.39 kJ mol^{-1}) for CO oxidation was found for Co_3O_4–$CuCo_2O_4$, which was about half that of the CuO catalyst (79.96 kJ mol^{-1}) (Fig. 4b). This suggested that the hybrid spinel bimetallic structure generated after constructing the MOF-on-MOF precursor was more favorable for CO low temperature oxidation than single metallic nanoparticles. Moreover, the hybrid Co_3O_4–$CuCo_2O_4$ composites had a competitively high TOF value (1.14×10^{-3} s^{-1}) at 90 °C, which is two orders of magnitude higher than CuO (1.24×10^{-6} s^{-1}) and superior to Co_3O_4 (0.305×10^{-3} s^{-1}) and $CuCo_2O_4$ (0.51×10^{-3} s^{-1}). The reduction behavior of different catalysts was investigated via H_2-TPR (Fig. S20, ESI†). Co_3O_4–$CuCo_2O_4$ had a strong reduction peak at 253 °C, which was attributed to both the reduction of Cu^{2+} to Cu^+ and Co^{3+} to Co^{2+}, and another peak at 296 °C was assigned to the reduction of Co^{2+} to Co. Compared with other catalysts, Co_3O_4–$CuCo_2O_4$ had a lower reduction temperature and exhibited better low temperature catalytic activity. The oxygen species in the catalysts were investigated via O_2-TPD (Fig. S21, ESI†), where the first desorption peak below 250 °C belonged to surface reactive oxygen that adsorbed on the oxygen vacancies formed by inter copper and cobalt interactions.[13] The following desorption peak in the range of 250–700 °C was assigned to the adsorption of oxygen defects on Co_3O_4–$CuCo_2O_4$. The relative front of the emerging peak position of Co_3O_4–$CuCo_2O_4$ indicates that the hybridized microflower was prone to forming oxygen defects.

In summary, we have successfully developed a facile and general exchange-extended growth method for constructing MOF-on-MOF architectures from different MOFs with distinct crystal topologies and components. The heteroarchitecture of the MOF precursors enabled Co_3O_4–$CuCo_2O_4$ to possess a larger surface area and abundant composition, which showed a much better performance (100% CO conversion at 100 °C) than the single-component CuBDC-derived catalyst and single-structure CuCoBDC-derived catalysts in low-temperature catalytic oxidation. More importantly, our strategy is universal for various MOFs matrices and can be expanded for the design and synthesis of extensive hybrid MOF systems that combine different physical and chemical properties on a large scale.

Conflicts of interest

There are no conflicts to declare.

Notes and references

1 (a) H. Furukawa, K. E. Cordova, M. O'Keeffe and O. M. Yaghi, *Science*, 2013, **341**, 1230444; (b) W. Li, Y. Zhang, C. Zhang, Q. Meng, Z. Xu, P. Su, Q. Li, C. Shen, Z. Fan, L. Qin and G. Zhang, *Nat. Commun.*, 2016, **7**, 11315; (c) V. Y. Mao, P. J. Milner, J.-H. Lee, A. C. Forse, E. J. Kim, R. L. Siegelman, C. M. McGuirk, L. B. Porter-Zasada, J. B. Neaton, J. A. Reimer and J. R. Long, *Angew. Chem., Int. Ed.*, 2020, **59**, 19468–19477; (d) H. Y. Yuan, N. X. Li, W. D. Fan, H. Cai and D. Zhao, *Adv. Sci.*, 2022, **9**, 2104374; (e) L. Qin, R. Ru, J. Mao, Q. Meng, Z. Fan, X. Li and G. Zhang, *Appl. Catal., B*, 2020, **269**, 118754.
2 (a) Q. L. Zhu and Q. Xu, *Chem. Soc. Rev.*, 2014, **43**, 5468–5512; (b) K. G. Liu, Z. Sharifzadeh, F. Rouhani, M. Ghorbanloo and A. Morsali, *Coord. Chem. Rev.*, 2021, **436**, 213827; (c) G. Boix, X. Han, I. Imaz and D. Maspoch, *ACS Appl. Mater. Interfaces*, 2021, **13**, 17835–17843; (d) Y. Hou, Y. L. Liang, P. C. Shi, Y. B. Huang and R. Cao, *Appl. Catal., B*, 2020, **271**, 118929; (e) J. Chun, S. Kang, N. Park, E. J. Park, X. Jin, K.-D. Kim, H. O. Seo, S. M. Lee, H. J. Kim and W. H. Kwon, *J. Am. Chem. Soc.*, 2014, **136**, 6786–6789; (f) L. Chai, J. Pan, Y. Hu, J. Qian and M. Hong, *Small*, 2021, **17**, 2100607; (g) C. Liu, Q. Sun, L. N. Lin, J. Wang, C. Q. Zhang, C. H. Xia, T. Bao, J. J. Wan, R. Huang, J. Zou and C. Z. Yu, *Nat. Commun.*, 2020, **11**, 4971.
3 (a) K. Shen, L. Zhang, X. Chen, L. Liu, D. Zhang, Y. Han, J. Chen, J. Long, R. Luque and Y. Li, *Science*, 2018, **359**, 206–210; (b) X. G. Wang, H. Cheng and X. Z. Zhang, *Nano Res.*, 2021, **15**, 4693–4699; (c) D. Kim, G. Lee, S. Oh and M. Oh, *Chem. Commun.*, 2019, **55**, 43–46; (d) P. Deria, J. E. Mondloch, O. Karagiaridi, W. Bury, J. T. Hupp and O. K. Farha, *Chem. Soc. Rev.*, 2014, **43**, 5896–5912; (e) X. Jiang, R. Q. Fan, J. Zhang, X. K. Fang, T. C. Sun, K. Zhu, X. S. Zhou, Y. D. Xu and Y. L. Yang, *Chem. Eng. J.*, 2022, **436**, 135236; (f) Y. Gu, Y. n Wu, L. Li, W. Chen, F. Li and S. Kitagawa, *Angew. Chem., Int. Ed.*, 2017, **56**, 15658–15662.
4 D. Kim, G. Lee, S. Oh and M. Oh, *Chem. Commun.*, 2019, **55**, 43–46.
5 Q. W. Zhang, Z. B. Yang, B. H. Chen and X. Liang, *Chem. Commun.*, 2019, **55**, 8450–8453.
6 (a) D. S. Liu, M. N. Li, X. C. Li, F. J. Ren, P. Sun and L. C. Zhou, *Chem. Eng. J.*, 2020, **387**, 124008; (b) J. Y. Cai, Y. Z. Zhuang, Y. Chen, L. Q. Xiao, Y. L. Zhao, X. C. Jiang, L. X. Hou and Z. H. Li, *ChemCatChem*, 2020, **12**, 6241–6247.
7 S. Mo, S. Li, H. Xiao, H. He, Y. Xue, M. Zhang, Q. Ren, B. Chen, Y. Chen and D. Ye, *Catal. Sci. Technol.*, 2018, **8**, 1663–1676.
8 L. Qin, Z. Xu, Y. Zheng, C. Li, J. Mao and G. Zhang, *Adv. Funct. Mater.*, 2020, **30**, 1910257.
9 X. L. Zhou, J. C. Dong, Y. H. Zhu, L. M. Liu, Y. Jiao, H. Li, Y. Han, K. Davey, Q. Xu, Y. Zheng and S.-Z. Qiao, *J. Am. Chem. Soc.*, 2021, **143**, 6681–6690.
10 M. Wang, J. X. Liu, C. M. Guo, X. S. Gao, C. H. Gong, Y. Wang, B. Liu, X. X. Li, G. G. Gurzadyan and L. C. Sun, *J. Mater. Chem. A*, 2018, **6**, 4768–4775.
11 Y. L. Zhu, W. Du, Q. L. Zhang, H. Yang, Q. Zong, Q. Q. Wang, Z. Zhou and J. H. Zhan, *Chem. Commun.*, 2020, **56**, 13848–13851.
12 L. Wang, H. Peng, W.-Q. Xie, S.-L. Shi, M.-W. Yuan, D. Zhao, S.-H. Wang and C. Chen, *Chem. Eng. Sci.*, 2022, **256**, 117675.
13 L. Wang, H. Peng, S.-L. Shi, Z. Hu, B.-Z. Zhang, S.-M. Ding, S.-H. Wang and C. Chen, *Appl. Surf. Sci.*, 2022, **573**, 151611.
14 X. Wang, W. Zhong and Y. Li, *Catal. Sci. Technol.*, 2015, **5**, 1014–1020.
15 C. J. Jia, M. Schwickardi, C. Weidenthaler, W. Schmidt, S. Korhonen, B. M. Weckhuysen and F. Schuth, *J. Am. Chem. Soc.*, 2011, **133**, 11279–11288.